Henning Bonart[1,*]
Johannes Jung[1]
Christian Kahle[2]
Jens-Uwe Repke[1]

Influence of Liquid Density and Surface Tension on the Pinning of Sliding Droplets on a Triangular Microstructure

Sliding droplets are crucial in many industrial applications. Examples are coating and separation processes involving multiple phases and liquid films. Often one can observe how a sliding droplet halts midstream on a solid surface. Wetting defects such as topographic structures can lead to a pinning of sliding droplets. In order to assess the influence of liquid density and surface tension on the pinning, direct numerical simulations are performed. After the model and its discretization are introduced, the solution is validated. Simulation results of gravity-driven droplets on inclined surfaces with structures in the size of the droplets are presented and the observed requirements for pinning a sliding droplet to a surface are discussed.

Keywords: Cahn-Hilliard-Navier-Stokes, Contact line dynamics, Drop phenomena, Phase field modeling, Pinning droplets

Received: January 14, 2019; *revised:* April 09, 2019; *accepted:* May 15, 2019

DOI: 10.1002/ceat.201900029

1 Introduction

Liquid droplets sliding along solid surfaces are a frequently observed phenomenon in nature, e.g., raindrops on a leaf, and in everyday situations like drops of water in a drinking glass. Furthermore, sliding droplets, and most often the suppression of those, i.e., complete wetting of liquid films, are crucial in many industrial applications. Examples are coating or painting processes and the efficient operation of separation or reaction processes involving multiple phases and thin liquid films. Frequently, the solid surfaces contain a certain statistical roughness, e.g., corroding pipes in heat exchangers, or a regular texture with dimensions in the same order of magnitude as the liquid film thickness, e.g., structured packings in distillation and absorption processes. While letting droplets flow down such non-smooth surfaces, often one can observe how a sliding droplet halts midstream on the solid surface. If one or more following droplets coalesce with the pinned droplet or the surface is tilted it starts sliding again.

From existing research on the pinning of droplets with low or near zero velocity, it is well-known that wetting defects such as chemical sections with variable wettability or topographic structures can lead to a pinning of droplets [1, 2]. For the pinning on sharp corners, the famous Gibbs' inequality gives a relation between the edge angle and the contact angles [3–5]. In many studies on sliding droplets the solid surface is assumed to be a smooth and homogeneous surface [6–8]. The conditions for the detachment of pinned droplets from defects have been examined quite well [9–11]. However, research about the capture of sliding droplets on wetting defects is very rare. In [12] and [13], experiments respectively simulations were performed on the pinning of sliding droplets on chemical heterogeneities like a rapid change of the contact angle. The pinning on a topographic defect was researched by [14, 15]. In those works, however, the defect was very small compared to the droplet. In contrast, many technical applications possess geometrical structures in the size of the droplet. Subsequently, little information is available on the systematic design of such microstructures on surfaces, e.g., for structured high-performance packings in distillation and absorption.

Hence, in this work, numerical simulations are performed to assess the values of liquid density and surface tension which lead to the pinning of a sliding droplet. A thermodynamic consistent Cahn-Hilliard-Navier-Stokes model for different densities is adopted to calculate the two-phase flow; see Sect. 2. As the resulting model forms a very tightly coupled and nonlinear system of equations, the discretization and solution strategy is carefully selected to allow efficient and accurate simulations. The model and the implementation are validated in Sect. 3 with analytical data on the spreading of droplets as well as on static hysteresis. In the detailed simulations in Sect. 4, the evolution of the velocity of the droplet from zero to a maximum velocity as the droplet slides down the incline can be observed.

[1]Henning Bonart, Johannes Jung, Prof. Dr.-Ing. Jens-Uwe Repke
henning.bonart@tu-berlin.de
Technische Universität Berlin, Dynamik und Betrieb technischer Anlagen, Strasse des 17. Juni 135, 10623 Berlin, Germany.

[2]Dr. Christian Kahle
Technische Universität München, Zentrum Mathematik, Boltzmannstrasse 3, 85748 Garching, Germany.

2 Cahn-Hilliard-Navier-Stokes for Moving Contact Line Simulations

2.1 Moving Contact Lines

By accurately observing a sliding droplet which gets pinned on a microstructure, one can identify the so-called moving contact line as well as the contact angles as having a crucial influence. As illustrated in Fig. 1, the moving contact line, or contact point if a two-dimensional problem is observed, is the position where the gas-liquid interface intersects the solid surface. In the past, a plurality of experimental, numerical, and theoretical studies were conducted to understand and predict the behavior of moving contact lines. For details about liquids on surfaces see, e.g., the reviews given in [7, 16].

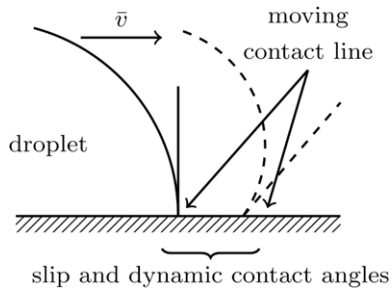

Figure 1. Illustration of the moving contact line and the contact angle of a sliding droplet on a solid surface.

Despite its crucial influence on the performance and efficient operation of a wide range of industrial applications, specific utilization of the moving contact line and contact angles is still rare. One of the main reasons for the rare research on moving contact lines in chemical engineering are the challenges in modeling and simulation of relevant flow configurations. Most often, the Volume-of-Fluid or Level-Set methods are applied for the simulation of two-phase flows. However, using these approaches together with the common no-slip boundary condition at the wall leads to a nonphysical singularity and a logarithmically diverging energy dissipation in the vicinity of the contact line [16, 17]. The result in these simulations is that a cell size-dependent slip at the contact line is implicitly included [18]. To circumvent this difficulty, in this work, the coupling of the incompressible Navier-Stokes equations with the Cahn-Hilliard equation is applied to calculate the two-phase flow [19].

As displayed in Fig. 2, compared to the sharp interface methods, this phase field method replaces the infinitely thin boundary between gas and liquid by a transition region with finite thickness. It describes the distribution of the different fluids by a smooth indicator function. It follows that all physical properties like density or viscosity vary continuously across the interface. Especially, the Cahn-Hilliard equation allows the contact line to move naturally on the solid surface due to a diffusive flux across the interface even if no-slip is assumed [19].

As summarized in the review by Wörner [20], the Cahn-Hilliard-Navier-Stokes (CHNS) equations can easily handle topological changes of the interface (merging and breakup) [21], the contact line can be accurately represented [22], and the interface is implicitly tracked without any prior knowledge of the position. Furthermore, one of the major advantages is that the formulation of the surface tension force in the Navier-Stokes (NS) equation exactly conserves both the surface tension energy and kinetic energy. This can reduce spurious currents, which are purely artificial velocities around the interface, to the level of the truncation error even for low capillary numbers [23, 24].

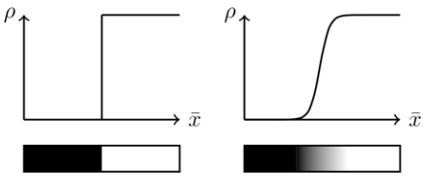

Figure 2. Comparison of the sharp and diffuse interface approach (DI). In DI, the density ρ changes gradually over the interface ($\bar{x}$ is the coordinate normal to the interface).

2.2 Model

The liquid droplet and the surrounding air are modeled as Newtonian, isotherm, immiscible, and incompressible fluids. In this work, the common incompressible, single-field Navier-Stokes (NS) equation is combined with the convective Cahn-Hilliard (CH) equation to describe the interface dynamics. To assess the spatial distribution of the two phases (liquid and gas), and thus the diffuse interface between them, with a single variable, an order parameter or phase field φ[1)] is introduced as:

$$\varphi(\mathrm{x},\mathrm{t}) = u_2 - u_1 = \begin{cases} -1, & \text{for pure phase 1 or } u_1 = 1 \\ +1, & \text{for pure phase 2 or } u_1 = 0 \end{cases} \tag{1}$$

in which u_1 and u_2 are the volume fractions of phase 1 (liquid) and 2 (gas). The further primal variables are given by the velocity field v, the pressure field p, and the chemical potential μ. In this work, the thermodynamically consistent diffuse interface model for large density differences between gas and liquid proposed in [25] is applied:

$$\rho\partial_\mathrm{t} v + (\rho v + J)\nabla v - \nabla(2\eta D v) + \nabla p = -\varphi\nabla\mu + \rho g \tag{2}$$

$$-\nabla v = 0 \tag{3}$$

$$\partial_\mathrm{t}\varphi + v\nabla\varphi - b\Delta\mu = 0 \tag{4}$$

$$-\sigma\varepsilon\Delta\varphi + \frac{\sigma}{\varepsilon}W'(\varphi) = \mu \tag{5}$$

which is closed with the boundary conditions, compare [26]:

$$v = 0 \tag{6}$$

$$\sigma\varepsilon\nabla\varphi\nu_\Omega + \gamma'(\varphi) = 0 \tag{7}$$

$$\nabla\mu\nu_\Omega = 0 \tag{8}$$

1) List of symbols at the end of the paper.

where ν_Ω denotes the outer unit normal on the computational domain. The abbreviations $J = -b\frac{\partial\rho}{\partial\varphi}\nabla\mu$, where b denotes the constant mobility of particles in the Cahn-Hilliard model, and $2D\nu = \nabla\nu + (\nabla\nu)^t$ are used. The gravitational acceleration is denoted by g and $p = p^{phys} - \mu\varphi$ is a shifted pressure, where p^{phys} means the physical pressure. The density function is denoted by $\rho \equiv \rho(\varphi) > 0$ and satisfies $\rho(-1) = \rho_1$ and $\rho(1) = \rho_2$, with ρ_1, ρ_2 being the constant densities of the two involved fluids. It is a linear function with respect to φ. Note that a linear relation might lead to negative densities if the density ratio is large [27]. Enforcing a positive density using a nonlinear relation, however, can lead to loss of mass during the simulation [8]. The viscosity function is $\eta \equiv \eta(\varphi) > 0$ and satisfies $\eta(-1) = \eta_1$ and $\eta(1) = \eta_2$, with η_1, η_2 being the viscosities of the involved fluids.

The function $W(\varphi)$ describes a dimensionless potential of double-well type. Here, it is chosen as:

$$W(\varphi) = \begin{cases} \frac{1}{4}(1-\varphi^2)^2, & \text{if } |\varphi| \le 1 \\ (|\varphi|-1)^2, & \text{else} \end{cases} \tag{9}$$

Moreover, the contact line energy is denoted by γ and interpolates smoothly between the solid-liquid and solid-gas surface energies. The expression for γ can be derived based on the assumption of equipartition of energy, i.e., $\frac{\varepsilon}{2}|\nabla\varphi|^2 \approx \frac{1}{\varepsilon}W(\varphi)$ [8]. It is given by:

$$\begin{aligned} \gamma'(\varphi) &= -\sigma_{12}\cos(\theta_s)c_W\sqrt{2W(\varphi)} \\ &= -\sqrt{2}\sigma\cos(\theta_s)\begin{cases} \frac{1}{2}(1-\varphi^2), & \text{if } |\varphi| \le 1 \\ (|\varphi|-1), & \text{else} \end{cases} \end{aligned} \tag{10}$$

where σ_{12} denotes the surface tension between phase 1 and 2 and θ_s is the static equilibrium contact angle between the solid and the interface and is measured in the liquid phase. In Fig. 3, the potentials W and γ are plotted. Finally, the constant ε is proportional to the thickness of the diffuse interface, while $\sigma = c_W\sigma_{12}$ denotes the scaled surface tension of the interface, where $c_W = 3/2\sqrt{2}$ is determined from the particular form of W; compare [8]. For details on the mathematical properties of W and γ see [8].

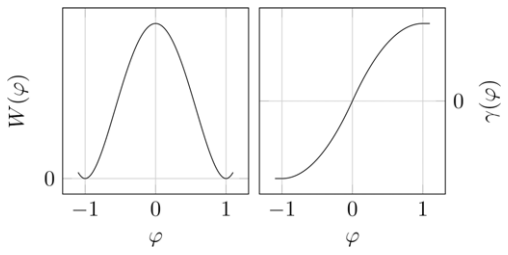

Figure 3. Bulk energy potential W and the surface energy potential γ.

The model (2)–(5) can be derived purely from thermodynamic principles [25]. Here, it is postulated that the system in the whole domain Ω with boundary $\partial\Omega$ can be described by the following sum of kinetic energy and Helmholtz free energy functional of Ginzburg-Landau type [28]:

$$E = \frac{1}{2}\int_\Omega \rho|v|^2 dx + \sigma\int_\Omega \in^{-1} W(\varphi) + \in |\nabla\varphi|^2 dx + \int_{\partial\Omega}\gamma ds \tag{11}$$

2.3 Implementation and Solution

The CHNS equations form a very tightly coupled and highly nonlinear system of four partial differential equations. Furthermore, the CH Eqs. (4) and (5) involve fourth-order derivatives respect to φ. Compared to the NS Eqs. (2) and (3), which involve only second-order derivatives, this complicates the numerical treatment [20]. In contrast to the more widespread segregated solution approach of the Cahn-Hilliard and Navier-Stokes equations, e.g., SIMPLE or PISO, in this paper, all the equations were solved coupled. This allows solving the system in a single solution step without any outer iterations. The equations were discretized using the finite-element method with Lagrange elements of first order for φ and μ and Taylor-Hood elements, i.e., second-order and first-order Lagrange elements, for v and p. The equations were implemented into the finite-element toolbox FEniCS [29]. For the solution of the resulting nonlinear equation system, PETSc [30] and SuperLU dist [31] were applied; see [8]. Further details on the applied discretization scheme and alternative time discretization schemes can be found in [8].

3 Validation against Analytical Solutions

In this section, the model and the implementation are compared to analytical results on droplet spreading and contact angle hysteresis. Validation against test cases without a moving contact line can be found in [32] and [8]. In these publications, liquid films flowing down a smooth surface as well as a bubble rising in a column were simulated and compared to analytical respectively benchmark results.

3.1 Droplets on Smooth and Homogeneous Surfaces

In this test case, a droplet with initial radius r_0 was placed on a solid surface with an initial contact angle of $\theta_0 = 90°$. Then, the equilibrium contact angle was set to a different contact angle between 30° and 150° and the simulation was performed until the droplet reached the new steady-state. Following [33, 34], neglecting gravity and assuming a perfectly smooth surface with a homogeneous contact angle, the equilibrium shape of a droplet can be exactly described by:

$$r_e = r_0\sqrt{\frac{\pi}{2(\theta_e - \sin(\theta_e)\cos(\theta_e))}} \tag{12}$$

$$l_e = 2r_e \sin(\theta_e) \tag{13}$$

$$h_e = r_e(1 - \cos(\theta_e)) \tag{14}$$

and the pressure difference between inside and outside of the droplet with

$$\Delta p = \sigma^{\text{phys}}/r_e \tag{15}$$

where σ^{phys} is the (not scaled) surface tension. In Fig. 4, the simulated height h_e, length l_e, and Δp are compared to the analytical equations. One can see that the results match almost perfectly for angles that are not too for away from 90°, and only for very small and very large angles a greater deviation between the analytical values and the experimentally obtained values was found. This probably appears due to mesh effects when the interface approaches the solid under a very flat angle.

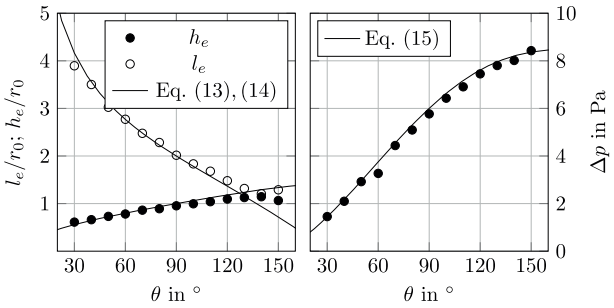

Figure 4. Length and height (left) and pressure drop across the interface (right) of a steady droplet for different contact angles θ. Analytical solutions given by Eqs. (13)–(15).

In a second step, the effect of gravity was included in the spreading of the droplet. A large gravity flattens the droplet. The effect is described by the Eötvös number:

$$Eo = \frac{(\rho_L - \rho_G) g r_0^2}{\sigma^{\text{phys}}} \tag{16}$$

which compares gravitational forces to surface tension forces. Here, ρ_L is the density of the droplet and ρ_G is the density of the other phase. For $Eo \to 0$ (surface tension dominates), the shape of the droplet follows the equations above whereas for $Eo \to \infty$ (gravity dominates) the height is given by:

$$h_\infty = \frac{2r_0}{\sqrt{Eo}} \sin\left(\frac{\theta_e}{2}\right) \tag{17}$$

In Fig. 5, the simulated height is displayed against different values of Eo. Again, it is obvious that the simulation matches the analytic equations very well.

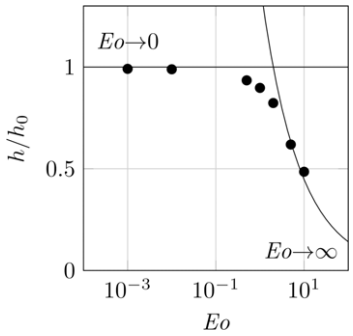

Figure 5. Normalized height of a steady droplet on a surface with θ = 90° for different *Eo*. Analytical solutions for Eo → 0 and Eo → ∞ given by Eqs. (14) and (17).

3.2 Pinning on an Inclined Surface due to Static Hysteresis

Until now, the solid surfaces were treated as perfectly smooth and ideal with a homogeneous contact angle. In practice, a solid surface exhibits physical or chemical defects which pin the contact line. In this case, the apparent contact angle of a static droplet on the surface deviates from the equilibrium contact angle. The contact angles at the rear and the front of the static droplet range from the receding angle θ_r to the advancing angle θ_a (Fig. 6).

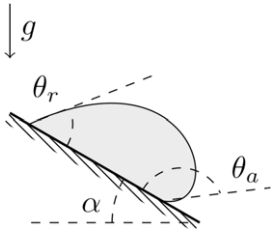

Figure 6. Setup of the validation case on pinning due to static hysteresis.

Applying the Young-Dupré equation at the front and the rear of the droplet results in a net force, which can balance gravity [35]. A balance of the involved forces along the direction of the surface leads to a condition for the pinning in dependence on the inclination of the surface [36]:

$$F_g = \text{mgcos}(\alpha) \quad \text{(weight)} \tag{18}$$

$$F_{h,s} \propto \left(\cos(\theta_{r,s}) - \cos(\theta_{a,s})\right) \quad \text{(static hys.)} \tag{19}$$

$$F_g \leq F_{h,s} \quad \text{(static pinning)} \tag{20}$$

$$Eo \leq \frac{\cos(\theta_r) - \cos(\theta_a)}{\sin(\alpha)} \tag{21}$$

In this work, the inhomogeneous solid surface was modeled by applying two different contact angles at the front and the rear of the droplet; see Fig. 6. The Eötvös number was set to *Eo* = 2.45 and the inclination angle of the surface was varied between 10° and 50°. The inset in Fig. 7 indicates that even if

the droplet is pinned, the shape of the droplet adapts to gravity. Note that this figure represents steady-state results and the droplet will not start moving again or even drip. In total 15 simulations were performed and the results are plotted in Fig. 7. In this figure, filled dots mean that the front and rear contact line of the droplet stayed pinned to the surface. The dashed line is the border between pinned and not pinned. It is calculated from condition Eq. (21) with its slope given by the Eötvös number Eo = 2.45. It is evident that the model and the implementation are able to predict the pinning due to the static hysteresis.

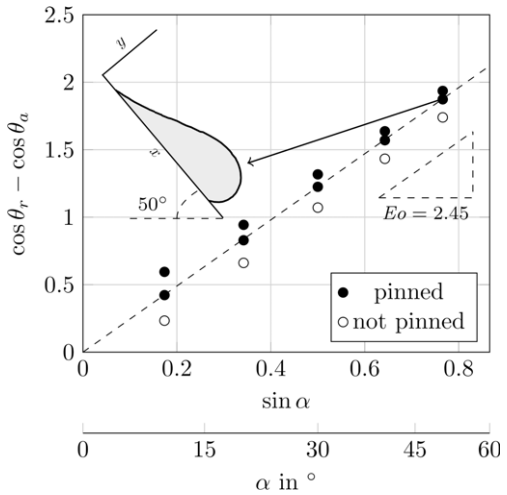

Figure 7. Results of the simulations on the pinning of a droplet due to static hysteresis. Exemplarily, the simulated shape of a pinned droplet hanging on a wall with inclination θ = 50° is shown.

4 Trapping of Droplets on a Microstructure in Dependence on Liquid Density and Surface Tension

In Fig. 8 (left), the domain and setup for the simulation case are illustrated. The surrounding walls were modeled using the boundary conditions Eqs. (6)–(8). Furthermore, a constant and homogeneous contact angle θ was specified at the walls for every simulation. As indicated in Fig. 8, a single liquid hemisphere surrounded by air was placed on the wall with a diameter l_d = 5 mm. The initial contact angle was always 90°. The distance between the droplet center and the center of the triangular obstacle was $2l_d$. The height and the base length of the triangular structure were $0.25h_d$ respectively $0.5h_d$, where h_d is the radius of the initial droplet or $0.5l_d$. In the present work, only a two-dimensional configuration was assumed but the methodology can be easily extended to fully three-dimensional droplets.

Tab. 1 states the physical properties of the liquids, the gas, and the solid surfaces. In this first exploratory study, the density and the surface tension were varied in a large range. The density of the liquid was chosen between 500 and 2000 kg m^{-3} and the surface tension was varied between 1 and 100 mN m^{-1}. A Latin

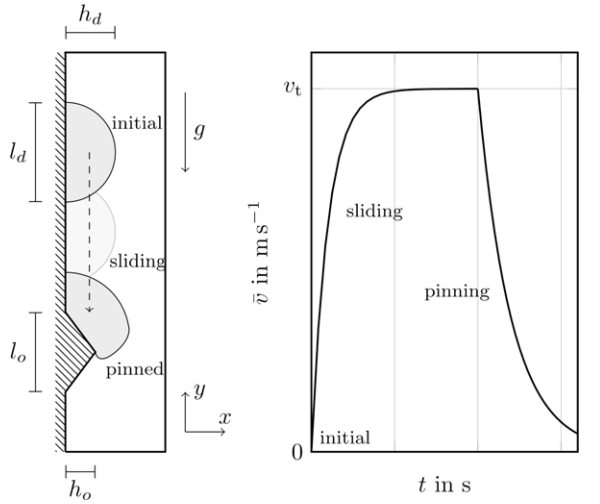

Figure 8. Configuration of pinning droplet test case and illustration of the development of the droplet shape and mean velocity.

Table 1. Physical parameters used in the pinning droplet simulations.

Parameter	Value
ρ_l [kg m^{-3}]	500– 2000
ρ_g [kg m^{-3}]	1.225
η_l [Pa s]	8.9×10^{-4}
η_g [Pa s]	1.81×10^{-5}
σ [mN m^{-1}]	1–100
θ	80°
l_0/l_d	0.5
h_0/h_d	0.5

hypercube sampling with 25 parameter combinations was performed. The numerical parameters ε and b were set to 1×10^{-4} m and 1×10^{-8} m^{3}s kg^{-1}. Following [34], the interfacial thickness ε was chosen to obtain a Cahn number $Ca = \varepsilon/l_d$ of 0.02 and the mobility was set to be $b = \varepsilon^2$. As long as the parameter values were in this order, changes of the values showed only a very low influence on the results. The time step was set to $\tau = 1\times10^{-3}$ s and an adaptive mesh with $h_{min} = 2\times10^{-5}$ m was utilized.

The development of the mean velocity of the droplet is indicated on the right of Fig. 8. After the start of the simulation the droplet starts sliding down the wall driven solely by gravity. During the simulation, the droplet spreads and adjusts its shape. Finally, the droplet reaches the microstructure, slows down at the sharp corner, and gets pinned (or not). The magnitude of the velocity inside the droplet during these different stages (from top to bottom) is demonstrated in Fig. 9 (left). Here, a droplet is shown which gets slowed down almost to a mean velocity of zero at the edge of the structure but not completely pinned. However, the pinned contact line and the large

apparent contact angel are clearly visible. In Fig. 9 (right), the phase field of the nearly pinned droplet is presented together with velocity streamlines. The diffuse interface between liquid and gas is thin but still observable.

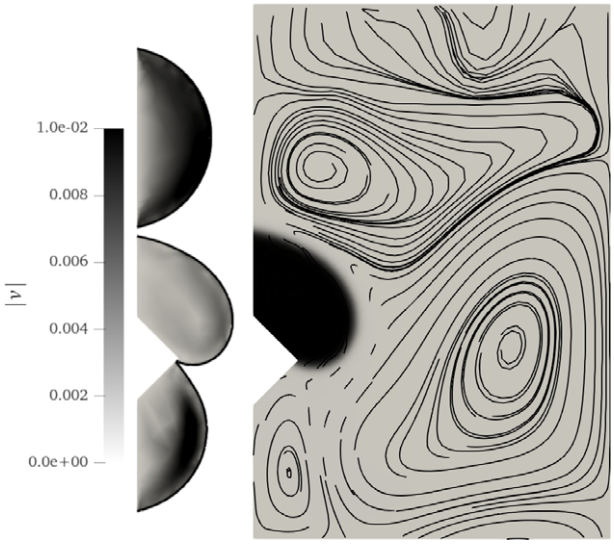

Figure 9. Magnitude of velocity inside the droplet at different stages: sliding, nearly pinning, sliding again (left). Phase field and velocity streamlines at the point of nearly pinning (right).

In total, 25 distinct parameter combinations for the range of liquid density and surface tension (see Tab. 1) were simulated. The results are displayed in the trapping diagram Fig. 10. Here, the x- and y-axes show the liquid density ρ_l respectively the surface tension σ. The filled dots represent the configuration with pinned droplets. For orientation, the configuration of water is marked. One notices that there is a clear distinction between pinning and not pinning. Furthermore, for lower densities a lower surface tension still leads to pinning whereas for higher densities a much higher surface tension is required to pin the sliding droplet. The dashed line represents a linear regression for the pinning in dependence on density and surface tension.

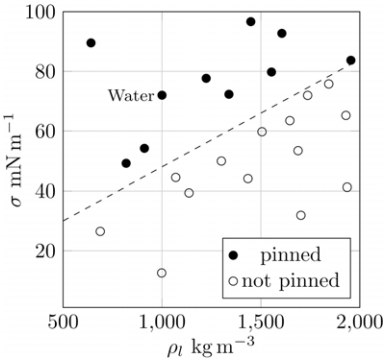

Figure 10. Trapping diagram with 25 distinct parameter combinations.

5 Conclusions and Outlook

In many technical applications liquid droplets slide over a solid surface. Most often, the surfaces possess geometrical structures in the size of the droplets and one can observe how a sliding droplet gets slowed down and pinned on the structure. As little information is available on the conditions of this trapping of sliding droplets, a first exploratory simulation study was performed in this paper. After an extensive validation against analytical results, detailed numerical simulations using the presented Cahn-Hilliard-Navier-Stokes model were performed for a wide range of liquid densities and surface tensions. It was found that both physical parameters have a significant impact on the pinning of sliding droplets. Interestingly, the border between pinning and not pinning shows a linear dependence between liquid density and surface tension. This work demonstrates that the model and implementation are capable to give insight into the pinning of sliding droplets. In future research, more detailed numerical studies with further parameter variations and surface microstructures will be conducted.

Acknowledgment

The first, second, and fourth author acknowledge the North-German Supercomputing Alliance (HLRN) for providing HPC resources that have contributed to the research results reported in this paper and thank the German Research Foundation (DFG) for the financial support within the project RE 1705/16-1. The third author gratefully acknowledges the support by the German Research Foundation (DFG) through the International Research Training Group IGDK 1754 "Optimization and Numerical Analysis for Partial Differential Equations with Nonsmooth Structures".

The authors have declared no conflict of interest.

Symbols used

b	[$m^3 s kg^{-1}$]	mobility
c_W	[–]	proportionality
Ca	[–]	Cahn number
Eo	[–]	Eötvös number
F	[N]	force
g	[$m s^{-2}$]	gravitational acceleration
h	[m]	height
l	[m]	length/diameter
p	[Pa]	pressure
r	[m]	radius
u	[–]	volume fraction
v	[$m s^{-1}$]	velocity
W	[–]	bulk potential

Greek letters

α	[°]	inclination angle
γ	[$J m^{-2}$]	contact line potential
Δ	[–]	difference

ε	[m]	interfacial thickness
η	[Pa s]	dynamic viscosity
θ	[°]	contact angle
μ	[kg m^{-1}s^{-2}]	chemical potential
ρ	[kg m^{-3}]	density
σ	[mN m^{-1}]	surface tension
τ	[s]	time step
φ	[–]	phase field
Ω	[–]	domain
$\partial\Omega$	[–]	boundary of domain

Subscripts

0	initial
1	phase one
2	phase two
d	droplet
e	equilibrium
g	gas
l	liquid
∞	infinity

Abbreviation

CHNS Cahn-Hilliard-Navier-Stokes

References

[1] J. M. Encarnación Escobar, E. Dietrich, S. Arscott, H. J. W. Zandvliet, X. Zhang, D. Lohse, *Langmuir* **2018**, *34 (19)*, 5396–5402. DOI: https://doi.org/10.1021/acs.langmuir. 8b00256

[2] W. Xu, C.-H. Choi, *Phys. Rev. Lett.* **2012**, *109 (2)*, 024504. DOI: https://doi.org/10.1103/PhysRevLett.109.024504

[3] J. W. Gibbs, *The Scientific Papers, Vol. 1*, Dover Publications, New York **1961**.

[4] D. C. Dyson, *Phys. Fluids* **1988**, *31*, 229–232. DOI: https://doi.org/10.1063/1.866851

[5] J. F. Oliver, C. Huh, S. G. Mason, *Colloid Interface Sci.* **1977**, *59 (3)*, 568–581. DOI: https://doi.org/10.1016/0021-9797(77)90052-2

[6] U. Thiele, K. Neuffer, M. Bestehorn, Y. Pomeau, M. G. Velarde, *Colloids Surf., A* **2002**, *206 (1–3)*, 87–104. DOI: https://doi.org/10.1016/S0927-7757(02)00082-1

[7] D. Bonn, J. Eggers, J. Indekeu, J. Meunier, E. Rolley, *Rev. Mod. Phys.* **2009**, *81 (2)*, 739–805. DOI: https://doi.org/10.1103/RevModPhys.81.739

[8] H. Bonart, C. Kahle, J.-U. Repke, *Comparison of Energy Stable Simulation of Moving Contact Line Problems using a Thermodynamically Consistent Cahn-Hilliard Navier-Stokes Model*, Preprint, **2018**, arXiv: 1809.06689.

[9] E. B. Dussan, V. R. Chow, *J. Fluid Mech.* **1983**, *137*, 1–29. DOI: https://doi.org/10.1017/S002211208300227X

[10] P. G. de Gennes, *Rev. Mod. Phys.* **1985**, *57 (3)*, 827–863. DOI: https://doi.org/10.1103/RevModPhys.57.827

[11] H. Ding, P. D. M. Spelt, *J. Fluid Mech.* **2008**, *599*, 341–362. DOI: https://doi.org/10.1017/S0022112008000190

[12] D. 't Mannetje, S. Ghosh, R. Lagraauw, S. Otten, A. Pit, C. Berendsen, J. Zeegers, D. van den Ende, F. Mugele, *Nat. Commun.* **2014**, *5 (1)*, 3559. DOI: https://doi.org/10.1038/ncomms4559

[13] A. Cavalli, M. Musterd, F. Mugele, *Phys. Rev. E* **2015**, *91 (2)*, 023013. DOI: https://doi.org/10.1103/PhysRevE.91.023013

[14] N. Savva, S. Kalliadasis, *J. Fluid Mech.* **2013**, *725*, 462–491. DOI: https://doi.org/10.1017/jfm.2013.201

[15] J. Park, S. Kumar, *Langmuir* **2017**, *33 (29)*, 7352–7363. DOI: https://doi.org/10.1021/acs.langmuir.7b01716

[16] J. H. Snoeijer, B. Andreotti, *Annu. Rev. Fluid Mech.* **2013**, *45 (1)*, 269–292. DOI: https://doi.org/10.1146/annurev-fluid-011212-140734

[17] C. Huh, L. E. Scriven, *J. Colloid Interface Sci.* **1971**, *35 (1)*, 85–101. DOI: https://doi.org/10.1016/0021-9797(71)90188-3

[18] M. Renardy, Y. Renardy, L. Jie, *J. Comput. Phys.* **2001**, *171 (1)*, 243–263. DOI: https://doi.org/10.1006/jcph.2001.6785

[19] D. Jacqmin, *J. Fluid Mech.* **2000**, *402*, S0022112099006874. DOI: https://doi.org/10.1017/S0022112099006874

[20] M. Wörner, *Microfluidics Nanofluidics* **2012**, *12 (6)*, 841–886. DOI: https://doi.org/10.1007/s10404-012-0940-8

[21] D. M. Anderson, G. B. McFadden, A. A. Wheeler, *Annu. Rev. Fluid Mech.* **1998**, *30 (1)*, 139–165. DOI: https://doi.org/10.1146/annurev.fluid.30.1.139

[22] P. Seppecher, *Int. J. Eng. Sci.* **1996**, *34 (9)*, 977–992. DOI: https://doi.org/10.1016/0020-7225(95)00141-7

[23] Q. He, K. Nobuhide, *Fluid Dyn. Res.* **2008**, *40 (7–8)*, 497–509. DOI: https://doi.org/10.1016/j.fluiddyn.2008.01.002

[24] F. Jamshidi, H. Heimel, M. Hasert, X. Cai, O. Deutschmann, H. Marschall, M. Wörner, *Comput. Phys. Commun.* **2018**, *236*, 72–85. DOI: https://doi.org/10.1016/j.cpc.2018.10.015

[25] H. Abels, H. Garcke, G. Grün, *Math. Model. Methods Appl. Sci.* **2012**, *22 (3)*, 1150013. DOI: https://doi.org/10.1142/S0218202511500138

[26] G. Grün, F. Guillén-Gonzáles, S. Metzger, *Commun. Comput. Phys.* **2016**, *19 (5)*, 1473–1502. DOI: https://doi.org/10.4208/cicp.scpde14.39s

[27] J. Kim, *Commun. Comput. Phys.* **2012**, *12 (3)*, 613–661. DOI: https://doi.org/10.4208/cicp.301110.040811a

[28] D. Jacqmin, *J. Comput. Phys.* **1999**, *155 (1)*, 96–127. DOI: https://doi.org/10.1006/jcph.1999.6332

[29] M. S. Alnæs, J. Blechta, J. Hake, A. Johansson, B. Kehlet, A. Logg, C. Richardson, J. Ring, M. E. Rognes, G. N. Wells, *Arch. Numer. Softw.* **2015**, *3 (100)*. DOI: https://doi.org/10.11588/ans.2015.100.20553

[30] S. Balay, J. Brown, K. Buschelman, V. Eijkhout, W. Gropp, D. Kaushik, M. Knepley, L. Curfman McInnes, B. Smith, H. Zhang, *PETSc Users Manual Revision 3.4*, Argonne National Laboratory, Argonne, IL **2014**. DOI: https://doi.org/10.2172/1178104

[31] X. S. Li, *ACM Trans. Math. Softw.* **2005**, *31 (3)*, 302–325. DOI: https://doi.org/10.1145/1089014.1089017

[32] H. Bonart, J.-U. Repke, *Chem. Eng. Trans.* **2018**, *69*, 61–66. DOI: https://doi.org/10.3303/CET1869011

[33] J.-B. Dupont, D. Legendre, *J. Comput. Phys.* **2010**, *229 (7)*, 2453–2478. DOI: https://doi.org/10.1016/j.jcp.2009.07.034

[34] X. Cai, H. Marschall, M. Wörner, O. Deutschmann, *Chem. Eng. Technol.* **2015**, *38 (11)*, 1985–1992. DOI: https://doi.org/10.1002/ceat.201500089

[35] H. B. Eral, D. J. C. M. 't Mannetje, J. M. Oh, *Colloid Polym. Sci.* **2013**, *291 (2)*, 247–260. DOI: https://doi.org/10.1007/s00396-012-2796-6

[36] B. Krasovitski, A. Marmur, *Langmuir* **2005**, *21 (9)*, 3881–3885. DOI: https://doi.org/10.1021/la0474565

